

# High density micro-pyramids with silicon nanowire array for photovoltaic applications

Rahman, Tasmiat; Navarro-Cia, Miguel; Fobelets, Kristel

DOI:

[10.1088/0957-4484/25/48/485202](https://doi.org/10.1088/0957-4484/25/48/485202)

License:

Creative Commons: Attribution (CC BY)

*Document Version*

Publisher's PDF, also known as Version of record

*Citation for published version (Harvard):*

Rahman, T, Navarro-Cia, M & Fobelets, K 2014, 'High density micro-pyramids with silicon nanowire array for photovoltaic applications', *Nanotechnology*, vol. 25, no. 48, 485202. <https://doi.org/10.1088/0957-4484/25/48/485202>

[Link to publication on Research at Birmingham portal](#)

## General rights

Unless a licence is specified above, all rights (including copyright and moral rights) in this document are retained by the authors and/or the copyright holders. The express permission of the copyright holder must be obtained for any use of this material other than for purposes permitted by law.

- Users may freely distribute the URL that is used to identify this publication.
- Users may download and/or print one copy of the publication from the University of Birmingham research portal for the purpose of private study or non-commercial research.
- User may use extracts from the document in line with the concept of 'fair dealing' under the Copyright, Designs and Patents Act 1988 (?)
- Users may not further distribute the material nor use it for the purposes of commercial gain.

Where a licence is displayed above, please note the terms and conditions of the licence govern your use of this document.

When citing, please reference the published version.

## Take down policy

While the University of Birmingham exercises care and attention in making items available there are rare occasions when an item has been uploaded in error or has been deemed to be commercially or otherwise sensitive.

If you believe that this is the case for this document, please contact [UBIRA@lists.bham.ac.uk](mailto:UBIRA@lists.bham.ac.uk) providing details and we will remove access to the work immediately and investigate.

## High density micro-pyramids with silicon nanowire array for photovoltaic applications

This content has been downloaded from IOPscience. Please scroll down to see the full text.

2014 Nanotechnology 25 485202

(<http://iopscience.iop.org/0957-4484/25/48/485202>)

View [the table of contents for this issue](#), or go to the [journal homepage](#) for more

Download details:

IP Address: 147.188.254.138

This content was downloaded on 16/12/2015 at 14:19

Please note that [terms and conditions apply](#).

# High density micro-pyramids with silicon nanowire array for photovoltaic applications

Tasmia Rahman, Miguel Navarro-Cía and Kristel Fobelets

Optical and Semiconductor Devices Group, Department of Electrical and Electronic Engineering, Imperial College London, London SW7 2BT, UK

E-mail: [tasmia.rahman07@imperial.ac.uk](mailto:tasmia.rahman07@imperial.ac.uk)

Received 9 June 2014, revised 11 September 2014

Accepted for publication 17 September 2014

Published 10 November 2014

## Abstract

We use a metal assisted chemical etch process to fabricate silicon nanowire arrays (SiNWAs) onto a dense periodic array of pyramids that are formed using an alkaline etch masked with an oxide layer. The hybrid micro-nano structure acts as an anti-reflective coating with experimental reflectivity below 1% over the visible and near-infrared spectral regions. This represents an improvement of up to 11 and 14 times compared to the pyramid array and SiNWAs on bulk, respectively. In addition to the experimental work, we optically simulate the hybrid structure using a commercial finite difference time domain package. The results of the optical simulations support our experimental work, illustrating a reduced reflectivity in the hybrid structure. The nanowire array increases the absorbed carrier density within the pyramid by providing a guided transition of the refractive index along the light path from air into the silicon. Furthermore, electrical simulations which take into account surface and Auger recombination show an efficiency increase for the hybrid structure of 56% over bulk, 11% over pyramid array and 8.5% over SiNWAs.

Keywords: nanofabrication, optics, SiNWA, FDTD, pyramids, photovoltaic

(Some figures may appear in colour only in the online journal)

## 1. Introduction

Crystalline silicon bulk solar cells suffer from undesirable high reflectivity because of silicon high permittivity (i.e., refractive index) and therefore exploring light trapping mechanisms to better exploit the energy harvested from the solar spectrum has grown considerable interest [1–7]. The standard solution in the current market is based on anti-reflective coatings made of silicon nitride (SiN<sub>x</sub>) [8]. This is commonly deposited using plasma enhanced chemical vapour deposition (PECVD). Alongside deposition methods, reflectivity can also be reduced by texturing the silicon surface which additionally enforces more scattering or light trapping. This has the added benefit in solar cell applications of increased p–n junction area. Texturing the surface can be

achieved via physical etching such as deep reactive ion etching (DRIE), or chemical etching in the form of alkalis such as potassium hydroxide (KOH) or acids such as hydrofluoric (HF) acid. Utilizing wet chemical etching to form textured surfaces is more cost effective for mass production and thus advantageous over PECVD and DRIE.

At a micro-scale, pyramids have been a well acknowledged light trapping mechanism in silicon solar cells [1–3]. A random array of pyramids are commonly processed by exposing mono-crystalline silicon into an alkaline solution. This leads to anisotropic etching in which the etch rate in the  $\langle 100 \rangle$  direction is far greater than the  $\langle 111 \rangle$ . When this occurs on a  $\langle 100 \rangle$  orientated wafer, a random array of pyramids of a large range in size will form. Many different etchants can be used, including aqueous solutions of tetramethylammonium hydroxide (TMAH) [2], sodium hydroxide (NaOH) [9] and KOH [10, 11]. The process is dependent primarily on the temperature, concentration (conc.) of alkali solution and also the surface quality of the silicon [10].



Content from this work may be used under the terms of the Creative Commons Attribution 3.0 licence. Any further distribution of this work must maintain attribution to the author(s) and the title of the work, journal citation and DOI.

At the sub-micron level, where the wavelength is at the same scale as the feature size, nanowire arrays have been utilized. Vertically aligned arrays of silicon nanowires (SiNWAs) are a growing technology field in photovoltaic (PV) cells [5–7]. The current PV industry is dominated by crystalline or poly-crystalline Si in a planar p–n junction configuration. The use of SiNWAs within this industry has shown great promise due to its application as an anti-reflective layer. In fact, with SiNWAs absorption can be increased to above 90% for wavelength range 400–800 nm [12, 13]. Furthermore, the fabrication process of SiNWAs can be of low-cost using metal assisted chemical etching (MACE) [14]. Other methods such as vapour liquid solid [15] growth as well as pattern and reactive ion etching (RIE) [16] also show promise, forming more ordered arrays than the MACE process but comes at a higher cost.

Here we use a combination of periodic pyramids and nanowires to form a hybrid structure that will have the two fold benefit of increased light absorption and junction area. Instead of using pyramids randomly organized via alkaline etching of bulk silicon, we fabricate a denser and periodic array using oxide masks. In this work, the pyramids periodicity varies from 4  $\mu\text{m}$  to 1.6  $\mu\text{m}$ , using an array of square oxide masks with widths of 2  $\mu\text{m}$ –800 nm. Vertical NWAs are then etched onto these pyramids using MACE to reduce the reflectivity further. The fabrication process of the hybrid structure is scalable and can be cost effective.

This paper is organized as follows. In section 2 we discuss the optical computational modelling method and simulation results. In section 3 we present and discuss the experimental procedures to fabricate these structures and the optical measured results. In section 4 we provide the electrical study of our structures taking into account recombination models. Finally, in section 5 we conclude our findings.

## 2. Simulation

We first simulate the SiNWA, pyramids and hybrid structures to identify the optical benefits of each of them in PV applications. Current approaches to compute nanoscale optics include finite difference time domain (FDTD) method [17], finite element method (FEM) [18] and rigorous coupled-wave analysis (RCWA) [19]. For the simulations performed in this work, a commercial FDTD package is used [20]. This has the benefit of efficient broadband 3D modelling over FEM and RCWA. Modelling of SiNWAs has shown an increase in light absorption, attributed to optical modes such as guided modes, Bloch modes and Fabry–Perot resonances [17, 18, 21]. Furthermore, it is shown that NWA optimization is dependent on geometrical properties.

In this paper we extend the aforementioned work and apply it to micro-nano surfaces. We provide a comprehensive analysis on the influence of the diameter, roughness and disorder to predict our experimental results. Furthermore, we show how such arrays can be added to pyramid structures to reduce the overall reflectivity and enhance photo-generation.

### 2.1. Method

FDTD calculates electromagnetic fields as a function of time and utilizes Fourier transforms to calculate the spectral response. We use a fitted model of multi-coefficients to represent tabulated refractive index ( $n, k$ ) data of silicon [22], and a plane-wave to model the solar spectrum with wavelength range 300–1000 nm. The plane-wave is injected from the top of the simulation domain. Periodic boundary conditions are applied in the  $x$  and  $y$  direction to replicate our array structures, whilst perfectly matched layers have been used in  $z$  direction (propagation direction) to absorb any reflected and transmitted fields. This effectively implies that our substrate and free-space are semi-infinite. Symmetric and antisymmetric boundaries have been used to reduce computation time when the unit cell allows it. A meshing algorithm is applied by the solver to form a mesh as a function of the material refractive index and interface structure. After a convergence analysis, the maximum and minimum length of our mesh cell is set to 14 and 2.5 nm, respectively. We also use a termination criteria of  $1 \times 10^{-5}$ , to ensure simulations end when the spectral response obtained by the Fourier transformation is valid. We measure the reflection ( $R$ ) data from a monitor placed at the top of our simulation domain. Since a semi-infinite lossy Si substrate is modelled, absorption is  $A = 1 - R$ . A power absorption ( $P_{\text{abs}}$ ) monitor is used to automatically map a spatial absorption profile by recording the electric field ( $E$ ) intensity and imaginary part of the permittivity ( $\epsilon$ ) [20]. This is proportional to the carrier generation ( $G$ ) by using the following relations:

$$P_{\text{abs}} = -0.5\omega|E|^2\text{imag}(\epsilon), \quad (1)$$

$$G = \frac{P_{\text{abs}}}{\hbar\omega}. \quad (2)$$

### 2.2. Results and discussion

The SiNWAs are modelled by placing cylinders of varying shapes onto a silicon cuboid block of 200 nm  $\times$  200 nm  $\times$  1  $\mu\text{m}$ . Figure 1 illustrates the reflectivity of a 500 nm long NWA with varying radius from 25 nm to 75 nm.

The features observed in this figure originate from the material properties of Si and the modes supported by the structure. The SiNW behaves like a circular dielectric waveguide whose eigenmodes are well-known [23]. For very small radius and large wavelength the effect of the SiNW is minimal and the reflection is similar to that of a bulk Si substrate. However, for small wavelength,  $\lambda$ , the SiNW is no longer insignificant and supports at least its fundamental mode. Hence, the reflectivity drops for  $\lambda < 400$  nm, because the excited mode is absorbed at that wavelength in Si. Furthermore, as the small radius SiNW supports only the fundamental mode, the structure of the spectrum is relatively simple. As the radius increases, absorption is triggered for the whole spectrum. Higher order modes emerge, governed by the radius of the NW, yielding additional structure in the spectrum. Their onset is red-shifted [23], as seen in the red-shift undergone by the dips (figure 1). The arrival of new

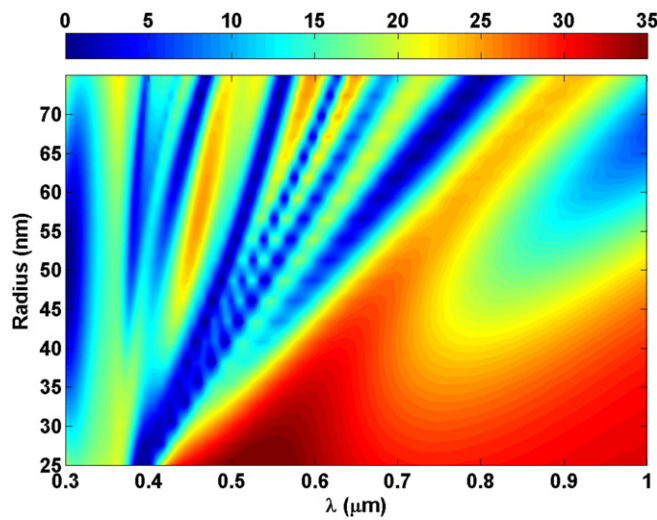


**Figure 1.** Reflectivity (%), represented by the colourbar, of various NWA radius as a function of wavelength.

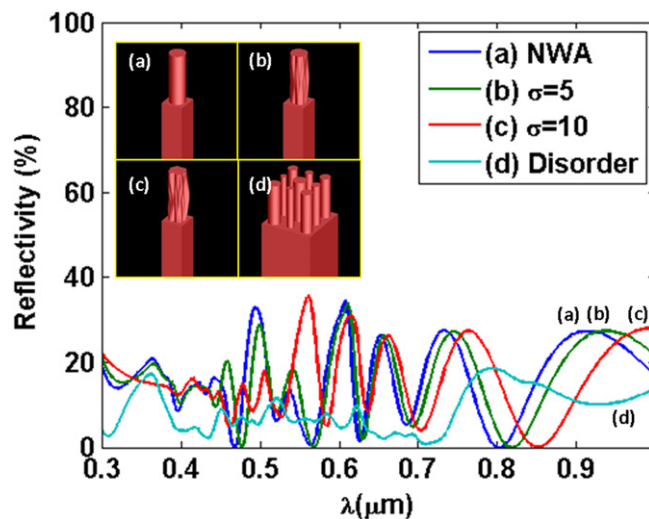


**Figure 2.** Reflectivity of SiNWs with varying roughness or disorder. (a): Perfect SiNWA; (b) and (c): rough SiNWAs and (d) is the pseudo disorder case.

modes also modifies the coupling between the incident plane-wave and the already existing modes, which are eventually absorbed. In this analysis we have neglected the interaction between modes of neighbouring SiNWs to give a simple physical insight. However, this assumption is arguably not valid for SiNWs with radius approaching the unit cell size. Hence, the difficulty to describe quantitatively the complex spectrum displayed on the top part of figure 1.

In figure 2, the effect of the SiNW surface roughness is investigated as well as the random variance of the NW radius, representative for SiNWs from the MACE process. As a reference, a SiNW of radius 75 nm and length of 500 nm is used (see inset (a) in figure 2). The roughness is modelled by a root-mean-squared height  $\sigma = 5$  and 10 with a correlation length  $L_c = 20$  nm in the  $x, y$  direction and 170 nm in the  $z$  direction, [20] (see inset (b) and (c) in figure 2). The hypothetical random variance of the radius in the fabricated

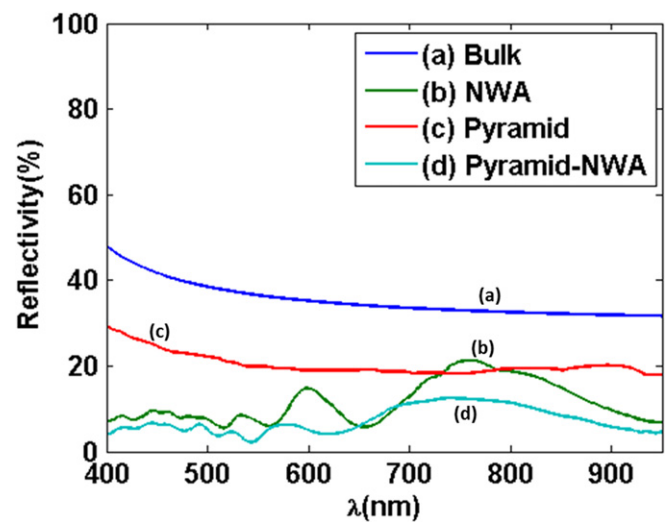


**Figure 3.** Reflectivity of bulk, pyramids, NWA and pyramids-NWA.

samples is modelled by a periodic macro-cell with 9 different SiNWs of radius 35, 40, 45, 50, 55, 60, 65, 70 and 75 nm (see inset (d) in figure 2). In the case of the rough and disordered NWAs, symmetric and antisymmetric boundaries are not used. From the comparison of smooth (a) and rough SiNW (b) and (c), it is evident that the addition of nm-scale roughness to the SiNW surface has a minor effect on the spectrum. There is an overall marginal red-shift of the spectrum as the roughness increases, which accounts for the effective larger diameter of the SiNWs for a specific transversal direction in  $x$ - $y$  plane. This can be correlated to the red-shift observed in figure 1 as the radius of the perfect circular cross-section increases. Regarding the reflectivity intensity, there is generally minimal change because the overall volume of Si does not change. In the case of the pseudo disorder (d), which models the disorder observed when producing NWs using the MACE process, a reduction in the overall reflectivity intensity is noticeable. This is an expected consequence of the superposition of the different spectra associated to each radius shown in figure 1.

Figure 3 compares the reflectivity of (a) bulk, (b) rough, quasi random SiNWAs, (c) periodic pyramid, and (d) hybrid structure. The pyramids used in these structures have a base width of  $2 \mu\text{m}$  and a height of  $1.6 \mu\text{m}$ . The reflectivity of the SiNWA is lower than the pyramid array, in accordance with literature [24, 25]. The pyramid structure behaves like a standard broadband absorber [26] as the pyramid geometry provides a continuous change in effective permittivity, and thus, tapers the impedance from that of free-space to bulk Si. In comparison, the impedance of the SiNWAs can be understood as a single step converter, which provides an intermediate impedance between that of free-space and bulk Si. In the hybrid structure an additional drop of the reflectivity is observed due to the combined impedance matching effect.

In figure 4 the total carrier generation rate at the middle cross-section plane for bulk, SiNWA, pyramids and hybrid structures is given. This is an integration of the power absorption due to an AM1.5 solar spectrum illumination. For



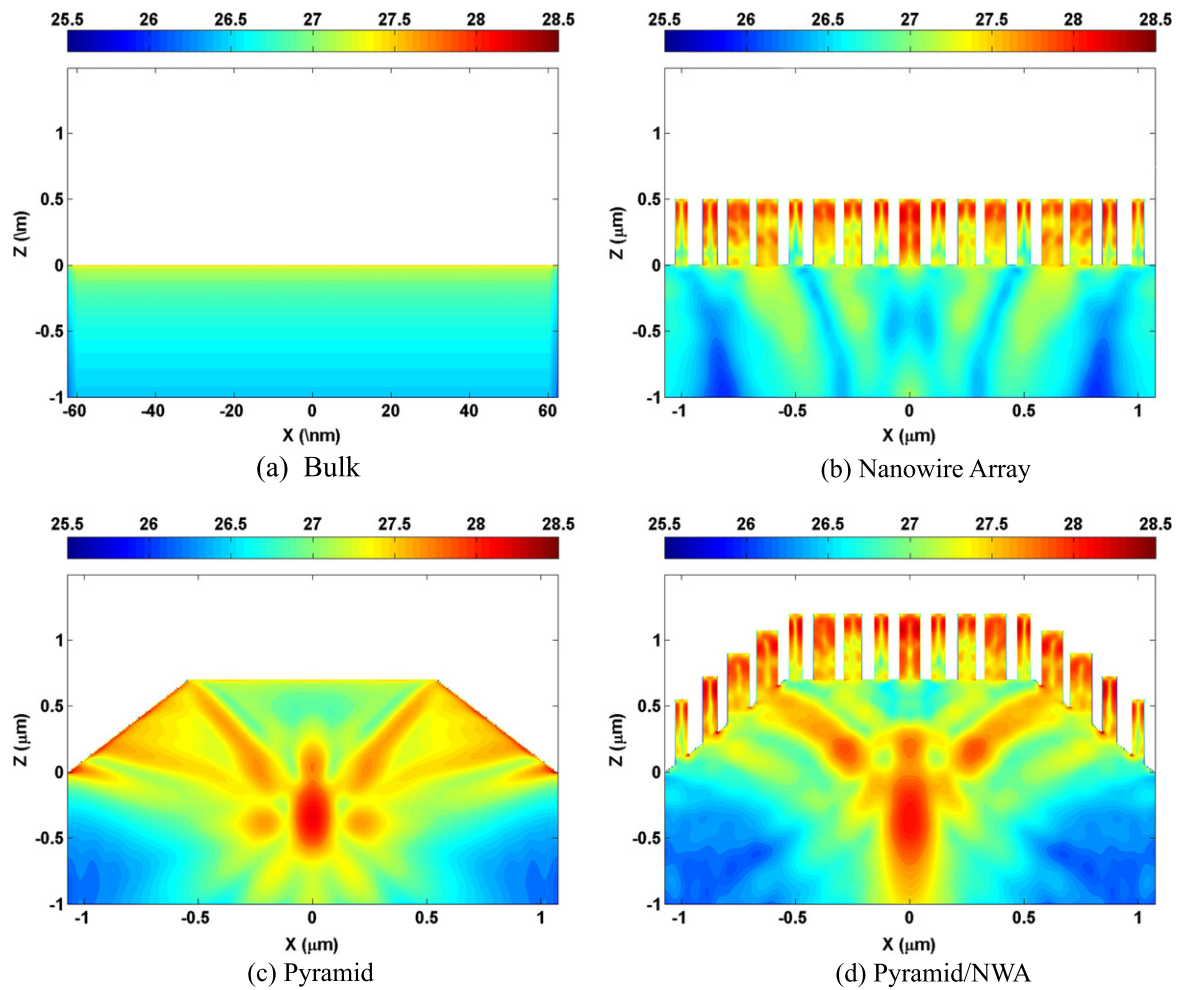


**Figure 4.** Spatial map of carrier generation rate ( $\text{m}^{-3} \text{s}^{-1}$ ), in logarithmic scale, of (a) bulk, (b) NWA, (c) pyramids and (d) pyramids-NWA.

a bare Si substrate, the absorption profile is uniform along  $x$ , has a maximum at the air–Si interface and decays along  $z$ , the propagation direction. When SiNWAs are introduced, most of the absorption happens in the SiNWAs because of the waveguide modes, but still significant absorption occurs in the Si substrate. For the pyramid case, in addition to the high carrier generation at the air–Si interface, an absorption hot spot arises at the centre of the pyramid. This absorption profile can be explained by the lens effect of the pyramid. The convex profile of the pyramid emulates a lens, concentrating the incoming rays into a focal region. Finally, for the hybrid structure, a superposition of the absorption profiles displayed by the SiNWAs and pyramids alone is observed. The high conc. of absorption in the SiNWAs should be seen as beneficial for solar cells, as the carrier generation will be high near the junction area.

### 3. Experiment

The fabrication of the hybrid structure consists of first, fabricating an array of pyramid using a combination of photolithography and alkaline etching, followed by a MACE process to fabricate a NWA on top.

KOH has been used to fabricate the pyramids because of its well controlled and reproducible behaviour [27]. The etch rate is dependent on crystal orientation, temperature and conc. of the etchant [28]. We have used a high conc. of KOH in order to obtain smooth surfaces. It has also been proven that isopropyl alcohol (IPA) improves the surface roughness due to increased wettability of the solution [29].

MACE is a popular NW preparation method for solar cell use, because it produces uniform NWs in terms of doping profile, crystal orientation, density, size, and shape [14]. MACE can be a one or two-step process using Ag or Au as catalysts [30–32]. We use a one step process because it allows better control of the etch rate when fabricating NWAs of sub-micron height [33].

Successful hybrid textured silicon surfaces have been fabricated using a combination of an alkaline etch to form a random pyramid array, followed by reaction ion etching to form the nanowire array [24] as well as MACE etching [6, 25, 34, 35]. Reflectivity of less than <3% in the wavelength range of 300–1000 nm have been reported from this texture.

In this paper we use photo lithography and an oxide mask for the alkaline etching of a periodic, dense array of pyramids with a MACE etched NWA on top. We will show that the

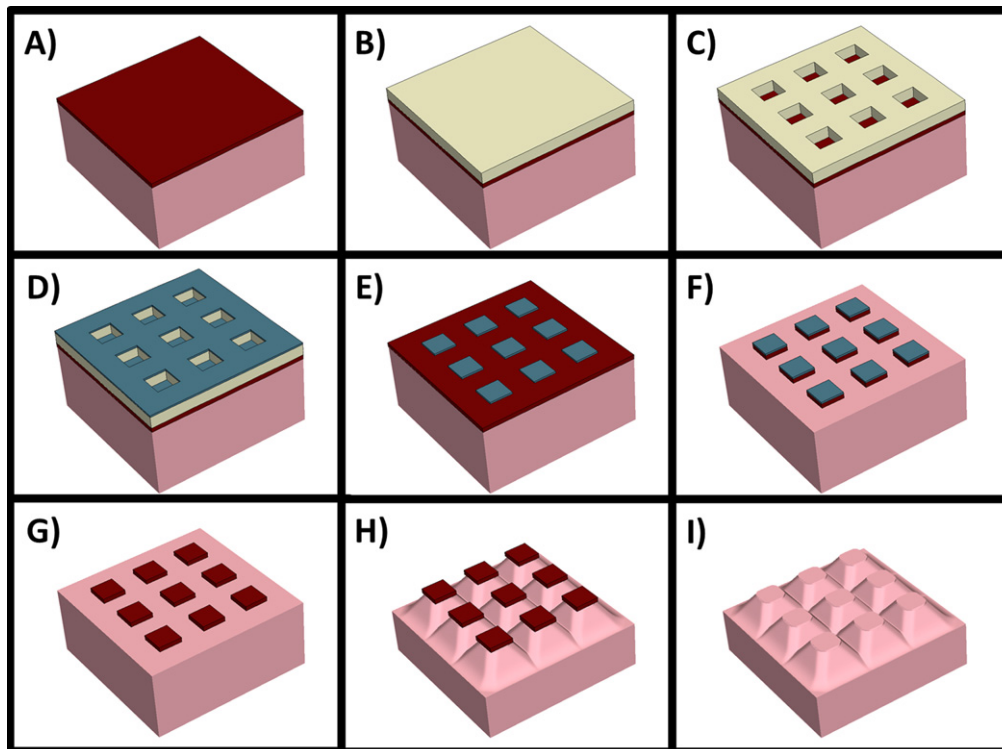


**Figure 5.** Schematic diagram of the process flow used to fabricate the dense array of pyramids. (A) Oxidation, (B) deposit resist, (C) expose and develop using mask, (D) deposit Cr, (E) strip resist, (F) etch oxide, (G) remove Cr, (H) KOH etch of Si, (I) BOE of oxide layer.

increase in density of the pyramids aids not only to light absorption but also increases junction area for PV use.

### 3.1. Method

The method we use for defining the periodic hybrid structures is as follows (see figure 5):

- (i) Clean the silicon wafer ( $\langle 100 \rangle$ , 1–10  $\Omega$  cm, phosphorous) by first ultrasonicing in IPA for 2 min. This is then followed by a piranha etch (3 : 1, conc.  $\text{H}_2\text{SO}_4$  : 30%  $\text{H}_2\text{O}_2$  solution) step for 15 min to remove small organic contamination.
- (ii) Oxidation: growth of approx. 150 nm thick  $\text{SiO}_2$  (1050  $^\circ\text{C}$ , 1 h ramp, 4 h dwell time, 1 l  $\text{h}^{-1}$   $\text{O}_2$ ).
- (iii) Lithography: deposit a 500 nm thin film of S1813. Bake on hotplate for 1 min at 115  $^\circ\text{C}$ . Expose for 9 s at 7.2  $\text{mJ cm}^{-2}$ . Develop in MF319 for 25 s. Evaporate a 80 nm thick Cr layer onto the sample. Lift off the photoresist by soaking in acetone and then sonication for 10 min. Plasma etch for 3 min (25 sccm Ar, 25 sccm  $\text{CHF}_3$ , 30 mTor, 20  $^\circ\text{C}$ , 200 W) and then buffered oxide etch (BOE) (6 : 1, 40%  $\text{NH}_4\text{F}$  : 49% HF) for approx. 20 s to produce the oxide mask. Use Cr etchant (1 : 1 : 8,  $\text{H}_8\text{N}_8\text{CeO}_{18}$ ,  $\text{HNO}_3$ ,  $\text{H}_2\text{O}$ ) to remove chrome mask.
- (iv) KOH etching: heat water bath to 80  $^\circ\text{C}$ . Mix 200 g KOH in 200 ml high performance liquid chromatography (HPLC) water, then add 20 ml IPA into beaker and place in water bath. 40% KOH + 10% IPA. Once KOH solution is at 80  $^\circ\text{C}$ , dip the sample into BOE for 3 s and then place the sample in etchant for desired time. Finally, rinse in water.

- (v) In order to form short NWAs we use a single step etch process which uses temperature as a catalyst. This involves a reaction of 3 M HF : 0.06 M  $\text{AgNO}_3$  in a 1 : 1 ratio at a temperature of 5  $^\circ\text{C}$ . By varying the time between 2–5 min we can achieve NWA lengths from sub-micron to approximately 3  $\mu\text{m}$ . The SiNWA is then placed into concentrated nitric acid. This step is important as it removes the remaining Ag on the samples.

### 3.2. Characterization

For optical measurements we use an ocean optics USB2000 + VIS-NIR-ES spectrometer, which uses a 2048 element CCD array with a detection range of 350–1000 nm. The light source is a HL-2000-FHSA. This has a wavelength range of 360–1700 nm and color temperature of 2960 K. For reflection measurements we make use of the reflection probe which emits light from an outer shell of six cores, and collects the reflected light from a larger inner core. The emission and collection of light is perpendicular to the sample, thereby collecting specular and diffuse reflections. In order to obtain a reference spectrum for normalization, we use a high-reflectivity specular reflectance standard. This mirror provides an 85–90% reflectance across a 250–800 nm range, and an 85–98% reflectance across the 800–2500 nm range.

### 3.3. Results and discussion

**3.3.1. Fabrication.** Figure 6 shows the SEM of the pyramid arrays formed from three different oxide masks of varying density. The parameters which define these pyramids are the

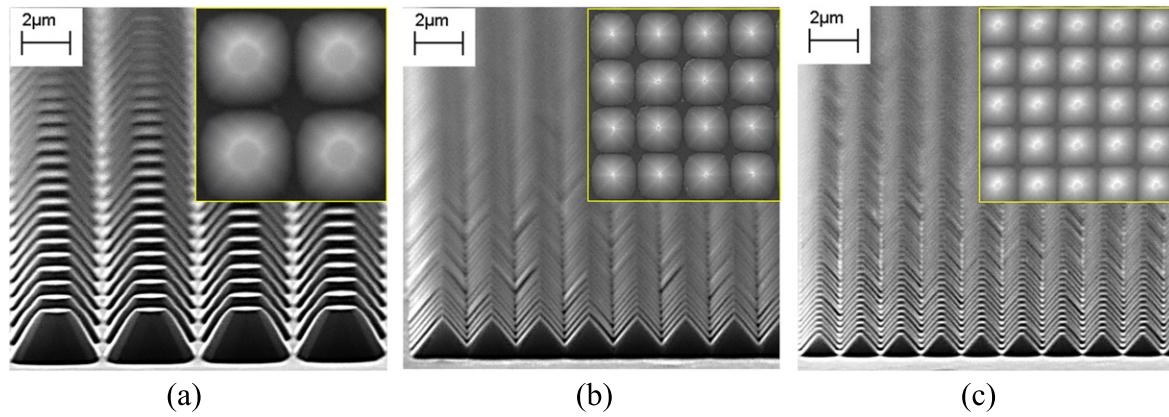


**Figure 6.** SEM image of pyramid array of varying densities: (a)  $W_{ox} = 2 \mu\text{m}$ , (b)  $W_{ox} = 1 \mu\text{m}$  and (c)  $W_{ox} = 0.8 \mu\text{m}$ . Inset give the top view for the same area in each case.

**Table 1.** Parameters defining the pyramid geometry for a given oxide mask size and etch time.

$W_{ox}(\mu\text{m})$	$t_e(\text{min})$	$W_b(\mu\text{m})$	$W_t(\mu\text{m})$	$L_p(\mu\text{m})$
2	2	3.7	1.1	2.15
1	2	2	0.1	1.6
0.8	1	1.5	0.3	0.9

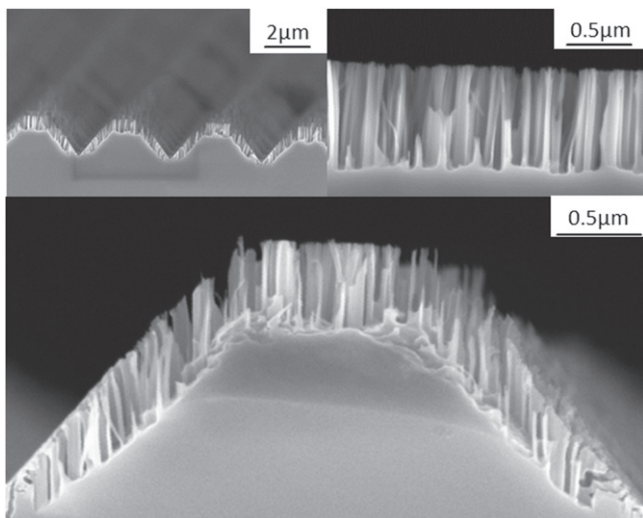


**Figure 7.** SEM image of a NWA on pyramids (top left and bottom) and a NWA on bulk (top right).

width and gap of the array of square oxide masks ( $W_{ox} = W_{gap}$ ), the KOH etch time ( $t_e$ ), the resulting length ( $L_p$ ), base width ( $W_b$ ) and top-face width ( $W_t$ ). The parameters of the different pyramid array are summarized in table 1.

In all cases the oxide mask is under-etched, resulting in multi-faceted pyramids. The effect of the under-etch is larger for the denser pyramid array, resulting in sharp tips rather than flat-faced tops. The quality of the pyramid formation is dependent on the quality of the surface prior to etching. The crucial steps included a buffered HF dip prior to etching as well as the presence of IPA in the alkaline solution.

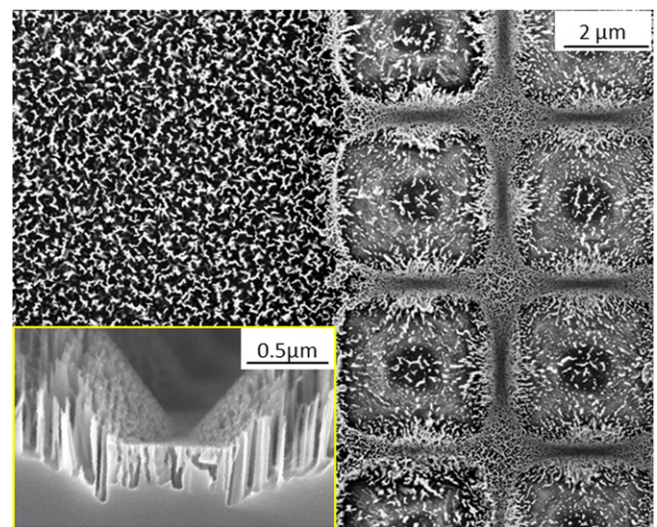


**Figure 8.** SEM images illustrating NWA formation in bulk and hybrid region (top) and also at the intersect between hybrid structures (bottom left inset).

Figure 7 shows the results of NWA etching both on the pyramids as well as on the bulk region for an etch time of 3 min. The NWs etch into all faces of the pyramids and thereby creates a NWA surface whilst pushing the pyramid geometry deeper into the substrate. This is due to the  $\langle 100 \rangle$  plane etching perpendicular, whilst on the  $\langle 111 \rangle$  plane at  $45^\circ$ . The overall size of the hybrid structure is the same as the pyramid prior to MACE. The NWAs etch with a uniform skyline and are well aligned. However, the length of the NWA differs on the hybrid structure and the bulk region despite having the same etch time. The length of NWA on bulk is  $L_{NWA} \approx 1 \mu\text{m}$ , whilst on the hybrid structures only  $L_{NWA} \approx 500 \text{ nm}$ . Figure 8 shows the top view of the NWA formation on bulk and the hybrid region. The inset gives the side view at which two hybrid structures intersect. From this we observe that the valleys in-between the pyramids are more porous Si than NWAs. This indicates a different Ag nucleation dynamics in the presence of surface structuring. Figure 9 shows the formation of hybrid structures fabricated via 1 min MACE process, thereby observing the predominant



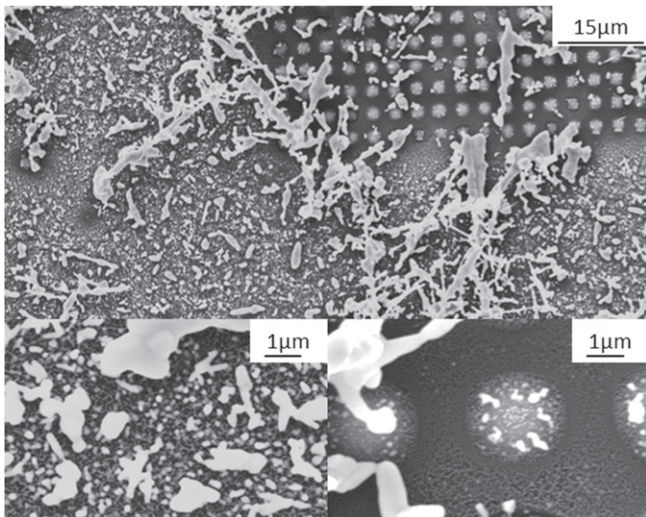


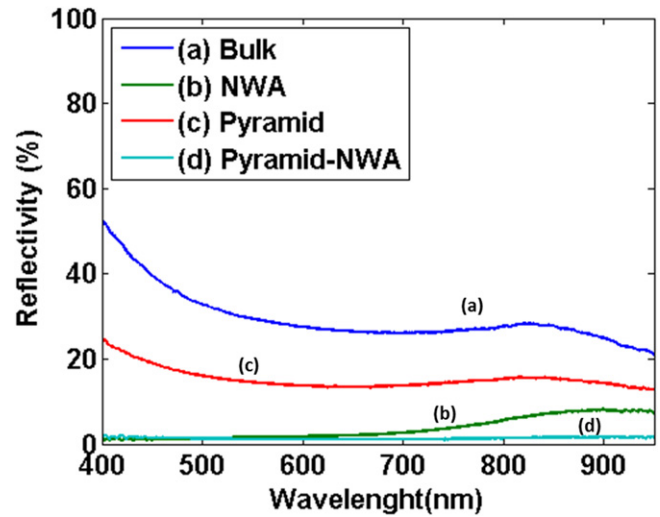
**Figure 9.** SEM images illustrating dendrite formation: in bulk and hybrid region (top), close up of bulk region (bottom left) and close up of hybrid region (bottom right).

effects of nucleation. We increase the area in-between the hybrid structures by applying a short KOH etch time to our least dense pyramid array. Whilst the bulk region contains dendrites of a large variety of sizes, the valleys in-between the hybrid structures contain minimal dendrites. The predominant dendrite formation in the hybrid region occurs on the top face of the pyramids, and the larger dendrites form by emerging with other dendrites formed on the top of adjacent pyramids. The reduced dendrite formation means less nucleation is occurring in the valleys and thus explains the formation of porous Si rather than NWA. Furthermore, the reduction in dendrites is also suggested as the cause for reduced etch rates in the hybrid structures. It has been reported that a lower surface area of dendrites results in inefficient capturing of silver ions for the redox reaction [36].

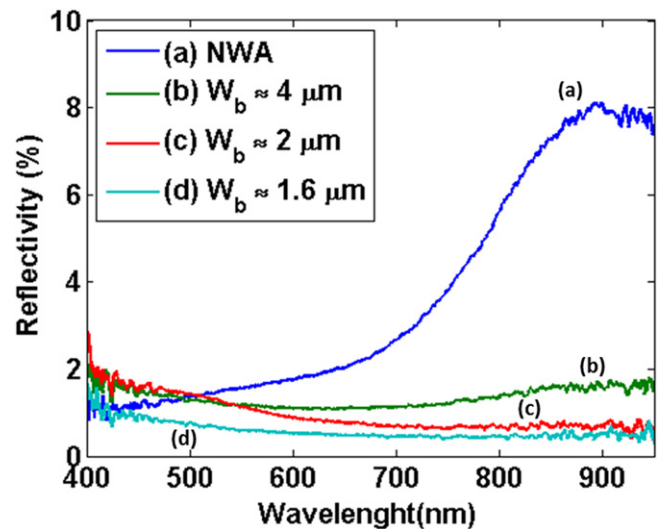
**3.3.2. Optical measurements.** Optical measurements were taken on pyramids of  $W_b \approx 4 \mu\text{m}$  and  $L_p \approx 2 \mu\text{m}$ ,  $W_b \approx 2 \mu\text{m}$  and  $L_p \approx 1.5 \mu\text{m}$  and  $W_b \approx 1.6 \mu\text{m}$  and  $L_p \approx 1 \mu\text{m}$ , and also their hybrid structures with  $L_{\text{NWA}} \approx 500 \text{ nm}$ .

Figure 10 shows the experimental reflection spectrum for the four cases discussed in section 2, namely (a) bulk Si, (b) SiNWAs, (c) pyramid array, and (d) hybrid structure. By comparison against the numerical results shown in figure 3, the agreement is excellent. As predicted, the lowest reflectivity is exhibited by the hybrid structure, whose benefit compared to SiNWAs is conspicuous for larger wavelengths. The lower reflectivity observed experimentally for SiNWAs and the hybrid structure stems from the larger heterogeneity of the fabricated samples in terms of radius size, which cannot be fully modelled because of computational limitations.

Finally, figure 11 shows the reflection spectrum for (a) SiNWAs and (b), (c), (d) hybrid structures with varying pyramid size, showing that increased density leads to reduced reflectivity. In accordance with figure 10 and the simulations,



**Figure 10.** Reflectivity of (a) bulk, (b) NWA, (c) pyramids and (d) pyramid-NWA structures.



**Figure 11.** Reflectivity of NWA and different density of hybrid structure.

figure 3, all hybrid structures outperform SiNWAs by repressing reflection in the higher wavelength range. Notice that the higher density hybrid structures have a shallower profile. This makes them more attractive for PV as the junction depth is more optimal. The better performance of the 2 and 1.6  $\mu\text{m}$  periodic hybrid structures with respect to the 4  $\mu\text{m}$  periodicity is a result of the improved tapered impedance matching. The 4  $\mu\text{m}$  periodic hybrid array fails to change the impedance smoothly from that of free-space as a result of its flat rather than pointed top.

#### 4. Electrical response

The PV characteristics of the different designs are modelled using the technology computer aided design (TCAD) package, Synopsys Sentaurus [37], which is an industry standard for device simulations [38–40]. This software package solves

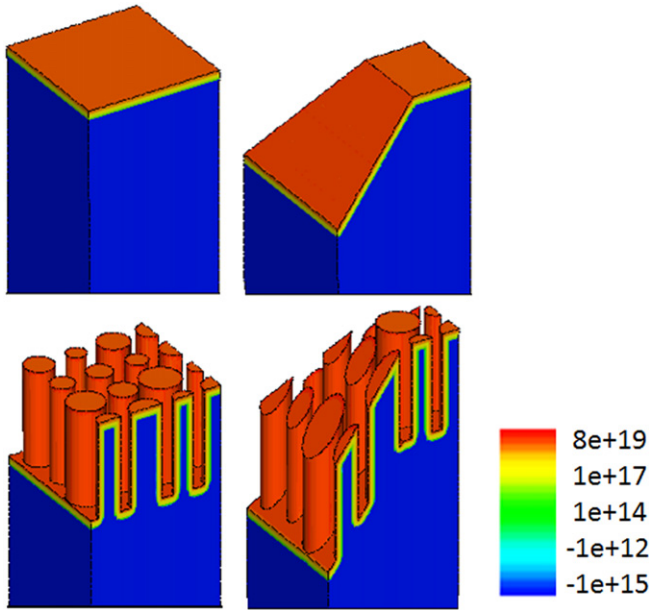


**Figure 12.** Net active ( $\text{cm}^{-3}$ ) doping profile of the four different structures.

the opto-electronic transport equations [41] in which the key computation in the device simulation is the electrostatic potential determined by mobile (electrons and holes), and stationary charges (ionized dopants and traps). The input data for these simulations is the geometry of the structures, the dopant profile, carrier generation profile and material parameters.

The structure is generated by simulating the silicon fabrication processes that include isotropic/anisotropic deposition and etching. The initial substrate is a  $\langle 100 \rangle$  silicon slab, 20  $\mu\text{m}$  thick and boron doping conc. of  $1 \times 10^{15} \text{ cm}^{-3}$ . The pyramid size formed after the etch has  $W_{\text{base}} = 1.6 \mu\text{m}$  and different NW radii (50–100 nm) to simulate the random character of real NWAs. The spin on dopant (SOD) process is simulated by depositing a layer of Phosphorous (P) dopant with a conc. of  $5 \times 10^{21} \text{ cm}^{-3}$ . P drive-in is done by annealing at 900  $^{\circ}\text{C}$  for 1 min. The oxide formed is removed by an anisotropic etch. The doping profiles of the various structures are given in figure 12. The junction depth is approximately 40 nm, which leaves the NWs with a core-shell structure. The carrier generation profile is solved using FDTD solutions from Lumerical [20], and integrated into Synopsys Sentaurus [37] to perform the electrical simulation under illumination. The structure is kept consistent in both softwares and the data is interpolated using Matlab, such that the Cartesian mesh from Lumerical is mapped to the Delaunay mesh in Sentaurus. The default Si material parameters are used [41], as well as the mobility and recombination models that have particular significance in PV simulations. The doping dependent mobility model takes into account impurity scattering in doped materials [41]. Shockley–Read–Hall (SRH) and Auger recombination, prevalent in high surface area and highly doped structures, are also accounted for [41]. The SRH

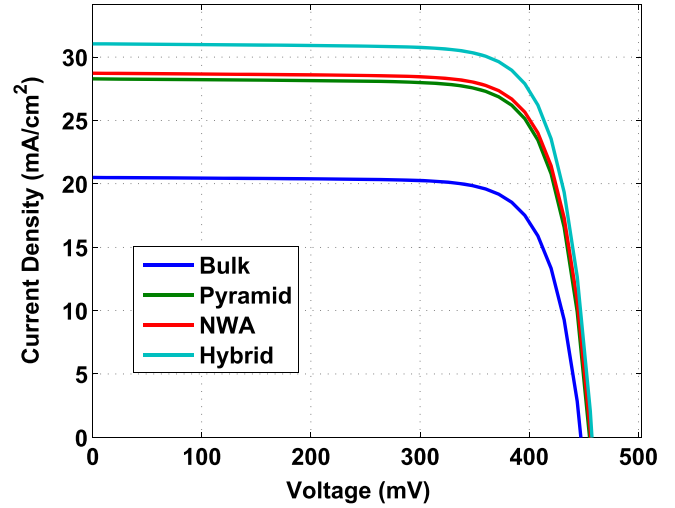


**Figure 13.** Current–voltage characteristics of the various structures under AM1.5 illumination.

recombination at the surface is defined as [41]:

$$R_{\text{surf,net}}^{\text{SRH}} = \frac{np - n_{i,\text{eff}}^2}{(n + n_1)/s_p + (p + p_1)/s_n}, \quad (3)$$

where:  $n_1 = n_{i,\text{eff}} e^{E_{\text{trap}}/kT}$ ,  $p_1 = p_{i,\text{eff}} e^{-E_{\text{trap}}/kT}$ ,  $n_{i,\text{eff}}$  is the intrinsic carrier conc.,  $E_{\text{trap}}$  is the difference between the defect level and intrinsic level,  $k$  the Boltzmann constant,  $T$  the temperature and  $s_{p,n}$  is surface recombination velocity (SRV). Due to the fabrication process, dangling bonds can exist at the surface, causing interface trap states (IFS) which are implicitly used in the equation (3).

In this work, we evaluate the influence of recombination and traps on the electrical performance of the proposed structures. Passivation of nanotextured silicon, via thermally grown oxide, PECVD  $\text{SiN}_x$  deposition or atomic layer deposition of  $\text{Al}_2\text{O}_3$  is well documented [6, 42–46]. Data obtained from these processing steps provide a lower and upper bound for SRV and IFS in these simulations. It is reported that SRV can reach as high as  $1 \times 10^5 \text{ cm s}^{-1}$  in unpassivated surfaces whilst values as low as  $10 \text{ cm s}^{-1}$  have been achieved with passivation [6, 42, 44–46]. Furthermore, for SiNWs, trap states of donor type have been identified [47]. These are positively charged when empty and are neutral when filled with an electron, with a cross-sectional area of  $1 \times 10^{-14} \text{ cm}^2$  [47]. The upper and lower bound for the conc. of these traps are  $1 \times 10^{11} \text{ cm}^{-2}$  for passivated and  $1 \times 10^{13} \text{ cm}^{-2}$  for unpassivated NWs, respectively [43].

The electrical characteristics for the passivated case are given in figure 13. This shows an increase in  $J_{\text{sc}}$  with respect to bulk for pyramid, NWA and hybrid structures. Furthermore, the hybrid structure has the highest  $J_{\text{sc}}$ , whilst the  $V_{\text{oc}}$  is similar for all. Table 2 summarizes the PV parameters for passivated ( $\text{SRV} = 10 \text{ cm s}^{-1}$ ,  $\text{IFS} = 1 \times 10^{11} \text{ cm}^{-2}$ ) and unpassivated ( $\text{SRV} = 1 \times 10^5 \text{ cm s}^{-1}$ ,  $\text{IFS} = 1 \times 10^{13} \text{ cm}^{-2}$ ) structures. Minimal change is observed for pyramid and bulk structures, however the NWA structures are influenced by the passivation process. For the passivated case, an efficiency

**Table 2.** The short-circuit current ( $J_{sc}$ ), open-circuit voltage ( $V_{oc}$ ) and efficiency ( $\eta$ ) of various structures, for both passivated (PS) and unpassivated (UPS).

	$J_{sc}$ (mA cm <sup>-2</sup> )		$V_{oc}$ (mV)		$\eta$ (%)	
	UPS	PS	UPS	PS	UPS	PS
Bulk	20.47	20.50	447.0	447.3	7.12	7.14
Pyramid	28.23	28.27	454.5	455.2	10.03	10.06
NWA	25.12	28.72	450.1	456.4	8.80	10.25
Hybrid	28.00	31.04	452.1	457.5	9.88	11.12

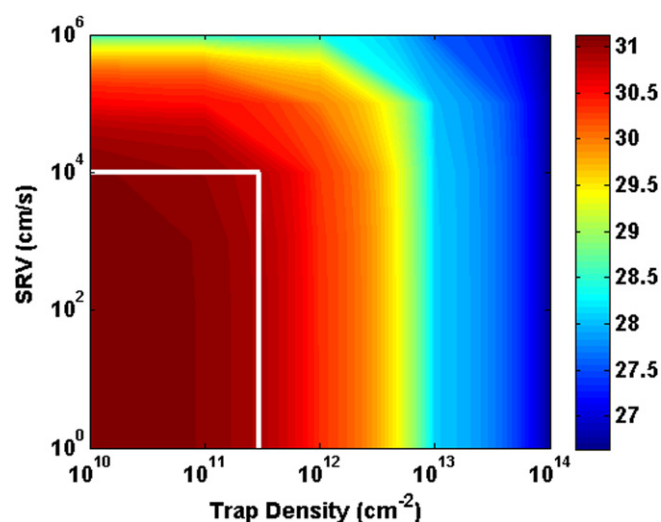


**Figure 14.** Influence of the surface recombination velocity (SRV) and the interface trap state density (IFS) on the short circuit current density  $J_{sc}$  (mA cm<sup>-2</sup>). The white line represents the threshold below which SRV and IFS are required to observe benefits in hybrid structures.

increase of 56% is observed from bulk to hybrid, whilst 8.5% increase is observed from NWA to hybrid. There is only a small increase between the pyramid to NWA case. This minimal increase is attributed to a trade off between lower recombination in the pyramid case and higher carrier generation observed in the NWA case.

Figure 14 shows  $J_{sc}$  for the full range of SRV and IFS concentrations. This shows the significant influence of passivation on  $J_{sc}$  in the hybrid structures, with  $J_{sc}$  gradually increasing as both IFS and SRV reduce. There is an acceleration in  $J_{sc}$  reduction as the SRV increases above  $1 \times 10^4$  cm s<sup>-1</sup> and IFS conc. above  $5 \times 10^{11}$  cm<sup>-2</sup>. Our results show that keeping recombination and traps below this threshold is required to benefit from the addition of NWAs to Si PV devices. These values have been achieved for passivated SiNWAs etched via the MACE process [6, 42, 45], which validates the feasibility of hybrid structures for efficiency improvement.

## 5. Conclusion

In this work we have simulated and measured the optical properties of hybrid micro-nano structures that consists of a dense array of Si pyramids with MACE SiNWAs. The NWA

on the pyramids etch perpendicular to the  $\langle 100 \rangle$  plane and at  $45^\circ$  to the  $\langle 111 \rangle$  plane, maintaining a uniform skyline and are well aligned. A reduced etch rate is observed in the hybrid region, due to the geometry limiting the Ag nucleation and thus dendrite formation. The hybrid structures with a pseudo-disordered NWA are modelled using a FDTD method. The results show that the combined pyramid-NWA structures outperform that of NWA and pyramid alone. The disordered NWA shows the lowest reflectivity by accumulating the absorption of the different modes present in a NWA with NWs of varying radius. The hybrid structure also shows an increase in carrier generation profile. This is due to the superposition of the lens-effect of the pyramid and the impedance matching via the NWA between free-space and bulk Si. Reflectivity is measured for bulk, NWA, pyramids and the hybrid structures. The results of our simulation agree well with the experimental data whereby the hybrid structures outperform both pyramids and NWA alone, reducing reflectivity below 1% for the case of  $1.6 \mu\text{m}$  periodicity. Furthermore, reflectivity reduces with increased density of arrays. The PV parameters of these structures are modelled using a commercial TCAD package. The results show a strong dependency on surface recombination whereby unpassivated structures do not translate an increase in carrier generation to a noticeable increase in efficiency. However, given surface passivation, the hybrid structure shows a significant improved efficiency of 56% over bulk, 11% over pyramid array and 8.5% over NWA.

## Acknowledgements

TR is supported by a EPSRC doctoral training award from Imperial College London. M N-C is supported by an Imperial College Junior Research Fellowship. The authors would like to thank the technical support provided by Lumerical Solutions Inc., Synopsys Inc. and Ocean Optics Inc.

## References

- [1] Blakers A W, Wang A, Milne A M, Zhao J and Green M A 1989 *Appl. Phys. Lett.* **55** 1363
- [2] Papet P, Nichiporuk O, Kaminski A, Rozier Y, Kraiem J, Lelievre J F, Chaumartin A, Fave A and Lemiti M 2006 *Sol. Energy Mater. Sol. Cells* **90** 2319–28
- [3] Dewan R, Vasilev I, Jovanov V and Knipp D 2011 *J. Appl. Phys.* **110** 013101
- [4] Fang H, Li X, Song S, Xu Y and Zhu J 2008 *Nanotechnology* **19** 255703
- [5] Zhang F, Song T and Sun B 2012 *Nanotechnology* **23** 194006
- [6] Lin X X, Hua X, Huang Z G and Shen W Z 2013 *Nanotechnology* **24** 235402
- [7] Stelzner T, Pietsch M, Andrä G, Falk F, Ose E and Christiansen S 2008 *Nanotechnology* **19** 295203
- [8] Raut H K, Ganesh V A, Nair A S and Ramakrishna S 2011 *Energy Environ. Sci.* **4** 3779
- [9] Singh P, Kumar R, Lal M, Singh S and Das B 2001 *Sol. Energy Mater. Sol. Cells* **70** 103–13
- [10] Palik E D, Glembocki O J, Heard I, Burno P S and Tenerz L 1991 *J. Appl. Phys.* **70** 3291



- [11] King D and Buck M 1991 *The Conf. Record of the 22nd IEEE Photovoltaic Specialists Conf.-1991* **303–08**
- [12] Kayes B M, Atwater H A and Lewis N S 2005 *J. Appl. Phys.* **97** 114302
- [13] Kelzenberg M D, Boettcher S W, Petykiewicz J A, Turner-Evans D B, Putnam M C, Warren E L, Spurgeon J M, Briggs R M, Lewis N S and Atwater H A 2010 *Nat. Mater.* **9** 239–44
- [14] Peng K Q and Lee S T 2011 *Adv. Mater.* **23** 198–215
- [15] Sunkara M K, Sharma S, Miranda R, Lian G and Dickey E C 2001 *Appl. Phys. Lett.* **79** 1546
- [16] Hung Y J, Lee S L, Thibeault B J and Coldren L 2011 *IEEE J. Quantum Electron.* **17** 869–77
- [17] Deinega A and John S 2012 *Opt. Lett.* **37** 112–4
- [18] Sturmberg B C P, Dossou K B, Botten L C, Asatryan A A, Poulton C G, de Sterke C M and McPhedran R C 2011 *Opt. Express* **19** A1067–81
- [19] Zanucoli M, Michallon J, Semehin I, Fiegna C, Kaminski-Cachopo A, Sangiorgi E and Vyurkov V 2013 *Energy Procedia* **38** 216–22
- [20] [www.lumerical.com/](http://www.lumerical.com/) accessed 1 June, 2014
- [21] Alaeian H, Atre A C and Dionne J A 2012 *J. Opt.* **14** 024006
- [22] Palik E D 1985 *Handbook of Optical Constants of Solids V* (Amsterdam: Elsevier) p 1
- [23] Balanis C A 2012 *Advanced Engineering Electromagnetics* (New York: Wiley)
- [24] Zhang X, Di Q, Zhu F, Sun G and Zhang H 2013 *J. Nanosci. Nanotechnol.* **13** 1539–42
- [25] Liu H C and Wang G J 2014 *Int. J. Photoenergy* **2014** 1–8
- [26] Hemming L H *Electromagnetic Anechoic Chambers: A Fundamental Design and Specification Guide* (New York: Wiley)
- [27] Schröder H, Obermeier E and Steckenborn A 1999 *J. Micromech. Microeng.* **9** 139–45
- [28] Muñoz D, Carreras P, Escarré J, Ibarz D, Martín de Nicolás S, Voz C, Asensi J and Bertomeu J 2009 *Thin Solid Films* **517** 3578–80
- [29] ZubeI I and Kramkowska M 2001 *Sensors Actuators A* **93** 138–47
- [30] Li X and Bohn P W 2000 *Appl. Phys. Lett.* **77** 2572
- [31] Sivakov V A, Bronstrup G, Pecz B, Berger A, Radnoczi G Z, Krause M and Christiansen S H 2010 *J. Phys. Chem. C* **114** 3798–803
- [32] Zhang M L, Peng K Q, Fan X, Jie J S, Zhang R Q, Lee S T and Wong N B 2008 *J. Phys. Chem. C* **112** 4444–50
- [33] Galopin E, Lemmens K, Piret G, Coffinier Y, Szunerits S and Boukherroub R 2008 *ECS Meeting Abstr.* **MA2008-02** 1810
- [34] He L, Lai D, Wang H, Jiang C and Rusli 2012 *Small* **8** 1664–8
- [35] Wang H P et al 2013 *ACS Nano* **7** 9325–35
- [36] Wee Q, Ho J W and Chua S J 2014 *ECS J. Solid State Sci. Technol.* **3** 192–7
- [37] [www.synopsys.com/Tools/TCAD/Pages/default.aspx](http://www.synopsys.com/Tools/TCAD/Pages/default.aspx) accessed 6 September, 2014
- [38] Kelzenberg M D, Turner-Evans D B, Putnam M C, Boettcher S W, Briggs R M, Baek J Y, Lewis N S and Atwater H A 2011 *Energy Environ. Sci.* **4** 866
- [39] Grandier J 2012 *J. Photonics Energy* **2** 024502
- [40] Deceglie M G, Ferry V E, Alivisatos A P and Atwater H A 2012 *Nano Lett.* **12** 2894–900
- [41] Synopsys Inc 2013 *Sentaurus Device User Guide* i-2013.12
- [42] Oh J, Yuan H C and Branz H M 2012 *Nat. Nanotechnology* **7** 743–8
- [43] Seo K i, Sharma S, Yasseri A A, Stewart D R and Kamins T I 2006 *Electrochem. Solid State Lett.* **9** G69
- [44] Dan Y, Seo K, Takei K, Meza J H, Javey A and Crozier K B 2011 *Nano Lett.* **11** 2527–32
- [45] Huang Z, Zhong S, Hua X, Lin X, Kong X, Dai N and Shen W 2014 *Prog. Photovolt., Res. Appl.* at press (DOI: [10.1002/pip.2506](https://doi.org/10.1002/pip.2506))
- [46] Alarcón-Illadó E, Mundet I C, Kiani A and Mallorquí A D 2014 *Nano Res.* at press (DOI: [10.1007/s12274-014-0551-7](https://doi.org/10.1007/s12274-014-0551-7))
- [47] Fobelets K, Meghani M and Li C 2014 *IEEE Trans. Nanotechnol.* at press (DOI: [10.1109/TNANO.2014.2349738](https://doi.org/10.1109/TNANO.2014.2349738))